AURORAL ARC ELECTRODYNAMICS: REVIEW AND OUTLOOK

Octav Marghitu
Institute for Space Sciences, Bucharest, Romania.

A necessary step towards unveiling the relationship between auroral phenomenology and magnetospheric processes is understanding the simplest and perhaps most widespread form of aurora, the discrete auroral arc. Current continuity and anisotropic Ohm's law in the ionosphere provide the basic tools to investigate the arc. After a general introduction into high-latitude and arc electrodynamics, three models are explored in more detail, corresponding to specific terms in the current closure equation: the 1D thin uniform arc (in altitude and longitude, respectively), the 2D thick uniform arc, and the 2D thin non-uniform arc. The examination of the 1D model is focused on the contributions made by polarization and field-aligned current (FAC) to the ionospheric current closure. The relative importance of the two mechanisms depends on the complete auroral current circuit, which is briefly addressed as well. The 2D thick uniform model enables a closer exploration of the Cowling effect, while the 2D thin non-uniform model concentrates on the conductance gradients along the arc. The 2D features are likely to be more prominent in the Harang region, where the formation of Cowling channels is related to substorms, while the termination of the large scale electrojets breaks the 1D symmetry. The various arc features are assembled together in a tentative 3D arc model, whose evolution is qualitatively described during the substorm cycle. Quantitative progress in the definition of the 3D arc is expected from newly developed ground based techniques and upcoming spacecraft missions.

1. INTRODUCTION

Aurora is the most spectacular effect of the complex interaction between the collisionless, hot and tenuous magnetospheric plasma, and the collisional, cold and dense ionospheric plasma. The typical setup of the auroral current circuit associated with the bright, discrete aurora, includes a magnetospheric generator, providing the required energy, the ionospheric–thermospheric load, where this energy is dissipated, and an auroral acceleration region (AAR), where a fraction of the electromagnetic field energy is converted into particle energy, precipitating further in the ionosphere. In the polar regions of the Earth, all these major constituents are connected together in a coupled magnetosphere–ionosphere–thermosphere (M–I–T) system by magnetic field lines and by the field-aligned currents (FAC) flowing along the field lines.

The I–T provides the passive load where the energy is dissipated, but it also feeds back to the magnetosphere, contributing actively to the M–I–T dynamics. The active I–T role in the formation of aurora started to be recognized already 40 years ago by *Atkinson* [1970], who was the first to describe the mechanism of the feedback instability, explored later by *Sato* [1978], *Lysak* [1986], and others. In this particular (and illustrative) case, the FAC modifies the ionospheric conductance, this changes the ionospheric current, and the divergence of the ionospheric current feeds back to the FAC. As pointed out by *Mauk and Bagenal* [this volume], such basic plasma processes have a universal character and auroral electrodynamics as investigated on Earth is relevant also for other planetary systems [e. g. *Ray and Ergun*, this volume; *Stallard*, this volume].

The epitome of the aurora is the auroral arc (Figure 1), perhaps the most widespread and "simplest" auroral form. The present review is intended to check how simple the "simple" arc is from an ionospheric perspective. Although some of the features to be discussed are rather general, the arc prototype to be explored is located in the nightside auroral oval, is rather wide, perhaps a few km to a few 10 km, and is reasonably steady, on a time scale of ∼10–100 s. A comprehensive view over the extended range of spatial and temporal scales covered by aurora is provided by other papers in this volume, from dynamic, thin filaments and arc systems [e. g. *Lanchester et al.*, this volume; *Kaeppler et al.*, this volume], to more slowly varying meso- and large-scale structures [e. g. *Lyons et al.*, this volume; *Zou et al.*, this volume].

Reviews of Geophysics, ???, /
pages 1–15
8755-1209/12/£15.00
Paper number

Figure 1. Quiet arc over Alaska. Credit: Jan Curtis.

Auroral arcs are typically described in terms of 1D, infinite stripes of increased ionospheric conductance. An upward FAC sheet above the arc is connected to a downward FAC sheet near the arc, while a divergence free electrojet (EJ) flows along the arc (Fig. 2a). In this case, both the FAC closure and the electrojet are driven by an electric field normal to the arc, as Pedersen and Hall current, respectively. The 1D configuration, including sometimes a (fairly small) tangential electric field, is often realized in the evening and morning sectors of the auroral oval, and was studied extensively in the past, based on radar, rocket, and satellite data [e. g. *de la Beaujardière et al.*, 1977; *Evans et al.*, 1977; *Marklund*, 1984]. As demonstrated by *Marklund* [1984], the 1D arc model is suitable for a detailed examination of the relative contributions of the polarization and FAC to the ionospheric current closure. The 1D arc current system is reproduced to a certain extent on oval scale, where downward and upward (thick) FAC sheets [*Iijima and Potemra*, 1976] are connected by meridional Pedersen currents [*Sugiura*, 1984], while large scale eastward and westward electrojets (EEJ and WEJ) flow along the oval in the evening and morning sector, respectively [*Baumjohann*, 1983].

In contrast to the 1D model, real arcs can exhibit also 2D features: the FAC can close not only normal to the arc but also along the arc, via both Pedersen and Hall currents, while the electric field can have a significant component along the arc (Fig. 2b). One possibility to extend the 1D model towards two dimensions is to relax the assumption that the electrojet is divergence free [*Marghitu et al.*, 2004, 2009, 2011]. Appropriate conditions for diverging electrojets, with impact also on arc scale, are realized in the (late) evening to midnight sector, in the so-called Harang region [*Harang*, 1946; *Heppner*, 1972; *Koskinen and Pulkkinen*, 1995], where both the EEJ and WEJ terminate. In the Harang region, the evening and morning sectors overlap, with the electric field and current pattern changing from evening-like to morning-like in west–east (zonal) and south–north (meridional) direction. The termination of the large scale electrojets implies coupling with both meridional currents [*Kamide*, 1978], in particular during quiet conditions, and FAC [*Baumjohann*, 1983; *Fuji et al.*, 1994], prevailing during disturbed conditions.

The 1D and 2D arc models introduced so far rely on a "thin" ionosphere, whose thickness is considered negligible as compared to the length of the magnetic field line in the magnetosphere. It turns out, however, that in order to properly consider the ionospheric current closure, one should also take into account the ionospheric thickness [*Amm et al.*, 2008]. One step in this direction [*Amm et al.*, 2011; *Fujii et al.*, 2011] is to assumes that the Hall and Pedersen current flow in thin layers at different altitudes (Figure 2c), consistent with the respective profiles of the Hall and Pedersen conductance (Figure 3). While originally Figure 2c was meant

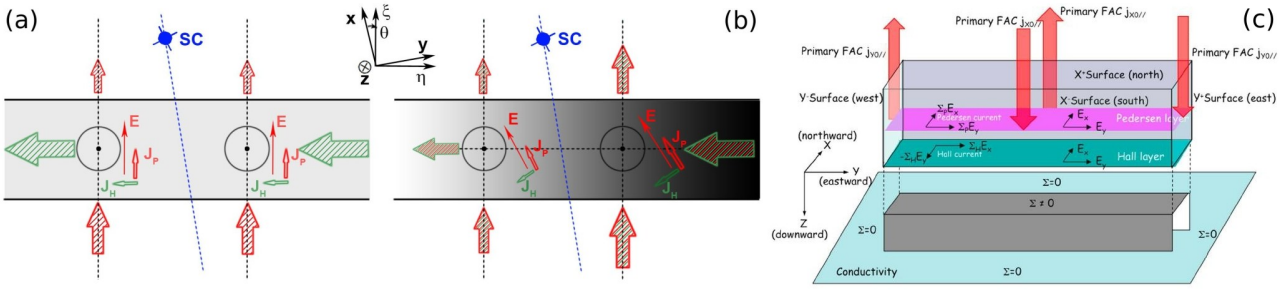

Figure 2. Thin uniform (a), thin non-uniform (b), and thick uniform (c) arc models. After *Marghitu et al.* [2011] (a, b) and *Fujii et al.* [2011] (c). In (a) and (b) the conductance, FAC, ionospheric electric field, and ionospheric current are indicated by the gray shade, circles, solid arrows, and hatched arrows respectively. Red and green show the Pedersen and Hall components of the current. For simplicity, the conductance variation in normal direction is not shown in (a) and (b) (but taken into account in the text). Note that in (a, b) (ξ, η) is associated with the arc and (x, y) with the satellite overpass, while in (c) (x, y) is associated with the arc.

to illustrate the electrodynamic configuration of a Cowling channel, it also appears appropriate to illustrate the "thick" arc. Note that despite the 3D view, the model in Figure 2c is uniform along the arc (even if, in this case, the arc is finite). The 2D arc models, illustrated by Figures 2b and 2c, appear to be complementary to each other, and may help to build up an as yet undeveloped 3D model of the arc.

After a short introduction into high-latitude ionospheric electrodynamics in Section 2, we shall explore in some detail the 1D thin uniform, 2D thick uniform, and 2D thin non-uniform arc, in Section 3, 4, and 5, respectively. A qualitative discussion of a 3D thick non-uniform arc model and its tentative evolution during the substorm cycle is provided in Section 6. The paper concludes by a concise summary in Section 7.

2. IONOSPHERIC ELECTRODYNAMICS IN THE AURORAL REGION

This section provides a brief summary of concepts and formulas to be used later in the paper. Comprehensive reviews of high-latitude ionospheric electrodynamics are available, for example, in *Kelley* [1989] or *Paschmann et al.* [2003].

2.1. General considerations

The current conduction in the ionosphere, contributed by both electrons and ions, is quantified by the anisotropic Ohm's law:

$$\mathbf{j} = \sigma_\parallel \mathbf{E'}_\parallel + \sigma_P \mathbf{E'}_\perp + \sigma_H \mathbf{e}_B \times \mathbf{E'}_\perp, \; \mathbf{e}_B = \mathbf{B}/B \quad (1)$$

where $\mathbf{B}$ is the magnetic field, $\sigma_\parallel$, σ_P, σ_H are respectively the parallel, Pedersen, and Hall conductivity, $\mathbf{j}_P = \sigma_P \mathbf{E'}_\perp$ and $\mathbf{j}_H = \sigma_H(\mathbf{e}_B \times \mathbf{E'}_\perp)$ are the Pedersen and Hall current. $\mathbf{E'}$ is the electric field in the reference system of the neutral atmosphere, $\mathbf{E'} = \mathbf{E} + \mathbf{u} \times \mathbf{B}$, with $\mathbf{u}$ the neutral wind velocity. The symbols "$\parallel$" and "$\perp$" are understood with respect to the magnetic field.

By taking into account the Lorentz force and the collisions with neutral atoms in the equations of motion for electrons and ions, $\sigma_\parallel$, σ_P, σ_H are found to have the following expressions [*Chapman*, 1956; *Brekke and Moen*, 1993]:

$$\begin{aligned} \sigma_\parallel &= \frac{ne}{B}\left(\frac{1}{\nu_{en}/\omega_{ge}} + \frac{1}{\nu_{in}/\omega_{gi}}\right) \\ \sigma_P &= \frac{ne}{B}\left(\frac{\nu_{en}/\omega_{ge}}{1+(\nu_{en}/\omega_{ge})^2} + \frac{\nu_{in}/\omega_{gi}}{1+(\nu_{in}/\omega_{gi})^2}\right) \\ \sigma_H &= \frac{ne}{B}\left(\frac{1}{1+(\nu_{en}/\omega_{ge})^2} - \frac{1}{1+(\nu_{in}/\omega_{gi})^2}\right) \end{aligned} \quad (2)$$

where n is the plasma density, ν_{in} and ν_{en} are the ion–neutral and electron–neutral collision frequencies, ω_{gi} and ω_{gi} are the ion and electron gyrofrequencies ($\omega_{ge,gi} = eB/m_{e,i}$). Because at E-layer altitudes, where the current flows, the mass difference between the main ion constituents, O_2^+ and NO^+, is small, the ionosphere can be represented by one equivalent ion species, with density $n_i = n_e = n$.

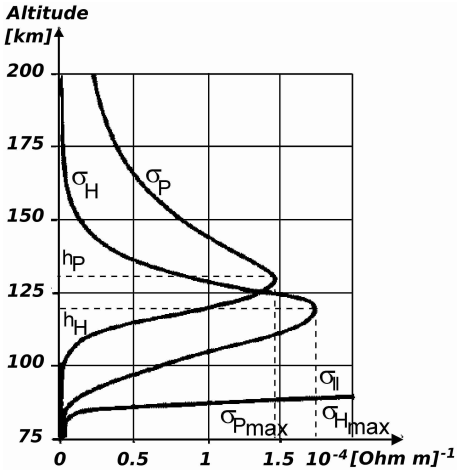

Figure 3. Altitudinal profiles of $\sigma_\parallel$, σ_P, and σ_H. After *Kertz* [1971]. While the numerical values are orientative and the details of the profiles can vary, the maximum Hall conductivity is always reached below the maximum Pedersen conductivity.

The variation of the conductivity with altitude, sketched in Figure 3, reflects both the changing plasma density, n, and the varying ratios of collision frequency to gyro-frequency, ν_{en}/ω_{ge} and ν_{in}/ω_{gi}. The combined effect of these factors leads to the concentration of the ionospheric current in the E-layer, where both plasma density and collision frequencies are high enough. At lower altitudes, in the D-layer, plasma density is rather low, while at higher altitudes, in the F-layer, the collision frequencies decrease too much. The parallel conductance takes very high values, so that for many applications the field-aligned potential drop in the ionosphere can be disregarded. Based on the respective contribution of the ion and electron term to σ_P and σ_H, one notes also that Pedersen current is dominated by ion transport at higher altitudes while the Hall current relies on electron flow at lower altitudes (as indicated by the maxima of σ_P and σ_H in Figure 3).

Since the I–T end of the M–I–T system is comparatively quite thin (a few 100 km compared to magnetic field lines of a few 10,000 km to several 100,000 km), the I–T is often regarded as a conductive thin layer. In addition, at auroral latitudes the magnetic field is almost normal to the ionosphere, within 10°–20°, and this small difference is in general neglected. Since the magnetic field lines can be considered as equipotentials, Ohm's law can be

integrated over the height of the ionosphere, resulting in:

$$\mathbf{J}_\perp = \Sigma_P \mathbf{E'}_\perp + \Sigma_H \mathbf{e}_B \times \mathbf{E'}_\perp \quad (3)$$

with

$$\Sigma_P = \int \sigma_P \, dz, \quad \Sigma_H = \int \sigma_H \, dz$$

the height-integrated Pedersen and Hall conductivities, or conductances. In the following we shall disregard the neutral winds, assuming that $\mathbf{E'} \equiv \mathbf{E}$, and omit the '$\perp$' symbol. Thus, by $\mathbf{E}$ and $\mathbf{J}$ we shall understand the 2D ionospheric electric field and current. Although neutral winds in the *E*-layer [e.g. *Brekke et al.*, 1994; *Nozawa and Brekke*, 1995] are associated with typically small electric fields, their influence can become significant when the auroral electric fields are also small. Since neutral wind information is often missing in auroral studies, this feature was not explored systematically, but it may receive more attention in the future (see Section 6).

The most dynamic factor in causing variations of the conductance is the plasma density. The gyrofrequencies, $\omega_{e,i}$, are essentially constant, while the collision frequencies, $\nu_{e,i}$, depend mainly on the neutral atmosphere [e. g. Appendix B.1 of *Kelley*, 1989], which varies on longer time scales. Thus, the variation of the conductance scales with the variation in n, whose evolution is governed by the continuity equation

$$\partial n/\partial t + \nabla \cdot (n\mathbf{v}) = q - \alpha(n^2 - n_0^2) \quad (4)$$

where $\mathbf{v}$ is the velocity of the plasma flow, α is the recombination coefficient, and n_0 is the background ionization. The source term q depends mainly on solar irradiation in the sunlit ionosphere and on the energy flux of the precipitating particles in the dark ionosphere. If the divergence of the ionization flux and the background ionization can be neglected, one obtains the steady-state solution

$$n(z) = \sqrt{\frac{q(z)}{\alpha(z)}} \quad (5)$$

valid on time scales longer than the recombination time, $\tau_{rec} = 1/\alpha n \simeq$1–100 s. While equation (5) ignores the respective contributions of the electrons and ions to the evolution of ionization, a careful analysis is required for a detailed understanding of this process [*Yoshikawa et al.*, 2011].

Proxies for the conductance induced by particle precipitation were provided e. g. by *Robinson et al.* [1987] (for electrons, Σ^e) and *Galand and Richmond* [2001] (for protons, Σ^p):

$$\Sigma_P^e = \frac{40\overline{E}}{16+\overline{E}^2}\Phi_E^{1/2} \quad (6) \qquad \Sigma_P^p = 5.7\Phi_E^{1/2} \quad (7)$$

$$\frac{\Sigma_H^e}{\Sigma_P^e} = 0.45\overline{E}^{0.85} \qquad \frac{\Sigma_H^p}{\Sigma_P^p} = 0.45\overline{E}^{0.3}$$

where Φ_E is the energy flux in mW/m^2 and $\overline{E}$ is the average energy in keV, $\overline{E} = \Phi_E/\Phi_N$, with Φ_N the number flux. The reader is warned against possible confusion between $\overline{E}$, the particle energy, and $\mathbf{E}$, the electric field. The total conductance scales with the total energy flux and can be approximated by:

$$\Sigma_{P,H} = \sqrt{\Sigma_{P,H}^{e^2} + \Sigma_{P,H}^{p^2}} \quad (8)$$

Besides Ohm's law and a conductance estimate, current closure equation is also required, in order to fully resolve the electrodynamics of the thin ionosphere. The secondary current driven by the electric field associated with the build up of polarization charge follows this build up almost instantaneously (on a time scale of the order $\epsilon_0/\sigma_P < 10^{-4}$ s), therefore charge conservation turns into current continuity:

$$\nabla \cdot \mathbf{j} = 0 \quad (9)$$

By integrating equation (9) over the height of the ionosphere, and assuming that no current can flow in the neutral atmosphere below, ionospheric current closure writes:

$$j_\parallel = \nabla \cdot \mathbf{J} = \nabla \cdot \mathbf{J}_P + \nabla \cdot \mathbf{J}_H \quad (10)$$

which can be further processed to

$$j_\parallel = \Sigma_P \nabla \cdot \mathbf{E} + \nabla\Sigma_P \cdot \mathbf{E} - (\nabla\Sigma_H \times \mathbf{E})_\parallel - \Sigma_H(\nabla \times \mathbf{E})_\parallel \quad (11)$$

The operator ∇ is understood in the plane of the 2D ionosphere. The ionospheric electric field is typically assumed to be electrostatic, and therefore the fourth term in equation (11) is neglected. However, as demonstrated by *Yoshikawa* [2002a, b], the inductive electric field is instrumental for feeding magnetic energy to the rotational part of the ionospheric current system (defined by $\nabla \cdot \mathbf{J}^{rot} = 0$ and dominated typically by the Hall current). As estimated by *Yoshikawa* [2002b], this process can take between a few seconds and a few minutes, depending on the spatial scale. For arc scales, the time is likely to be in the seconds range, therefore we shall disregard this effect in the following.

2.2. Arc related considerations

One can cast equation (11) into a form better suited for arc studies, by splitting the conductance

gradients and the electric field into normal and tangential components, ξ and η (see Figure 2):

$$j_{\parallel} = \Sigma_P \nabla \cdot \mathbf{E} + \partial\Sigma_P/\partial\xi\, E_\xi + \partial\Sigma_P/\partial\eta\, E_\eta - \partial\Sigma_H/\partial\xi\, E_\eta + \partial\Sigma_H/\partial\eta\, E_\xi \quad (12)$$

By disregarding the variation in η and the divergence of the Hall current, one is left, as a first approximation, with the simplest 1D arc model:

$$j_{\parallel} = dJ_{P_\xi}/d\xi = \Sigma_P\, dE_\xi/d\xi + d\Sigma_P/d\xi\, E_\xi \quad (13)$$

Equation (13) indicates that when the conductance has significant variations, as is always the case for auroral arcs, current continuity is achieved either by FAC ($d\Sigma_P/d\xi\, E_\xi = j_{\parallel}$), or by polarization ($d\Sigma_P/d\xi\, E_\xi = -\Sigma_P\, dE_\xi/d\xi$. The relationship between polarization and FAC in providing the ionospheric current closure for the 1D arc is investigated closer in Section 3.

As shown by equation (11), when the gradient of the Hall conductance, $\nabla\Sigma_H$, is not parallel to the electric field, there is also a Hall term contributing to the current closure. The contribution related to the gradient across the arc, fourth term on the right-hand side (r.h.s.) of equation (12), underlies the Cowling effect and can result also both in FAC and in accumulation of charges that generate a polarization electric field. While the Cowling effect can be incorporated in the 1D arc model, a proper treatment requires a thick ionosphere, taking into account the different altitudinal profiles of the Pedersen and Hall current. A simple configuration to achieve this goal, consisting of two thin layers at the altitudes where $\mathbf{J}_P$ and $\mathbf{J}_H$ reach their respective maxima [*Amm et al.*, 2011; *Fujii et al.*, 2011], will be addressed in Section 4.

Alternatively, one can add the second dimension in the plane of the thin ionosphere by considering also the variation of the conductance along the arc, third and fifth r.h.s. terms in equation (12). Since variations along the arc are still presumed to be significantly smaller than across the arc, the contribution of $\partial E_\eta/\partial\eta$ to the first r.h.s. term of equation (12) will be neglected. As discussed in Section 5, conductance variation along η can be incorporated by relaxing the assumption that the electrojet is divergence free. A technique to analyze the data and an event study will be presented to illustrate this case.

Before turning to the discussion of the arc models, it is appropriate to mention briefly the investigations of 2D aurora not relying on arc symmetry. While the elongated arc shape makes possible fairly complete approaches based on 1D data collected across the arc, e. g. by satellites, rockets, or radar scans, the exploration of 2D aurora requires 2D coverage of the observed data. For the time being, 2D coverage can be provided only by ground observations, most often on medium and large scale [see for example the reviews by *Untiedt and Baumjohann*, 1993; *Vanhamäki and Amm*, 2011]. Since rather recently, 2D dynamic small scale structures can be explored as well from the ground, by advanced optical and radar techniques [e. g. *Lanchester et al.*, this volume; *Semeter*, this volume].

3. THIN UNIFORM 1D ARC

The 1D arc model implies a thin ionosphere and variations of the physical parameters just across the arc. The consequences of the 1D current closure are explored first, and then some M–I coupling implications are briefly summarized.

3.1. Ionospheric current closure

With the FAC density expressed by Ampére's law, $j_{\parallel} = dH_\eta/d\xi$, equation 10 becomes:

$$\frac{d}{d\xi}(H_\eta - J_\xi) = 0 \quad (14)$$

which integrates to:

$$H_\eta(\xi) - J_\xi(\xi) = c_0 = H_\eta(\xi_0) - J_\xi(\xi_0) \equiv H_{\eta_0} - J_{\xi_0} \quad (15)$$

The reference point ξ_0 is located well outside of the arc, where the parameters take background values, while the point ξ is arbitrary. By using Ohm's law to replace J_ξ and J_{ξ_0}, one obtains the electric field at ξ as:

$$E_\xi = \frac{\Sigma_{P_0}}{\Sigma_P} E_{\xi_0} + \frac{\Sigma_H - \Sigma_{H_0}}{\Sigma_P} E_{\eta_0} + \frac{H_\eta - H_{\eta_0}}{\Sigma_P} \quad (16)$$

$E_\eta = E_{\eta_0}$ is constant because $\partial E_\eta/\partial\xi = \partial E_\xi/\partial\eta = 0$ and $\partial E_\eta/\partial\eta = 0$.

Equation (16) indicates that the ionospheric electric field associated with the arc is determined by two factors: the ionospheric polarization induced by the variation in conductance (first and second r.h.s. terms) and the field-aligned current (third r.h.s. term). The close relationship between FAC and polarization, as means to provide current continuity in the auroral ionosphere, was addressed theoretically already by *Boström* [1964] and *Coroniti and Kennel* [1972], together with possible M–I coupling implications (see Section 3.2). Later on, a systematic investigation of several arcs was performed by *Marklund* [1984]. He classified the observations according to the dominant current closure mechanism and was able to organize thus the rich variety of electric field signatures in the vicinity of auroral arcs. The numerical examination of equation (16), performed in Section 6.1 of *Paschmann et al.* [2003], provides a concise summary of these signatures, reproduced here in

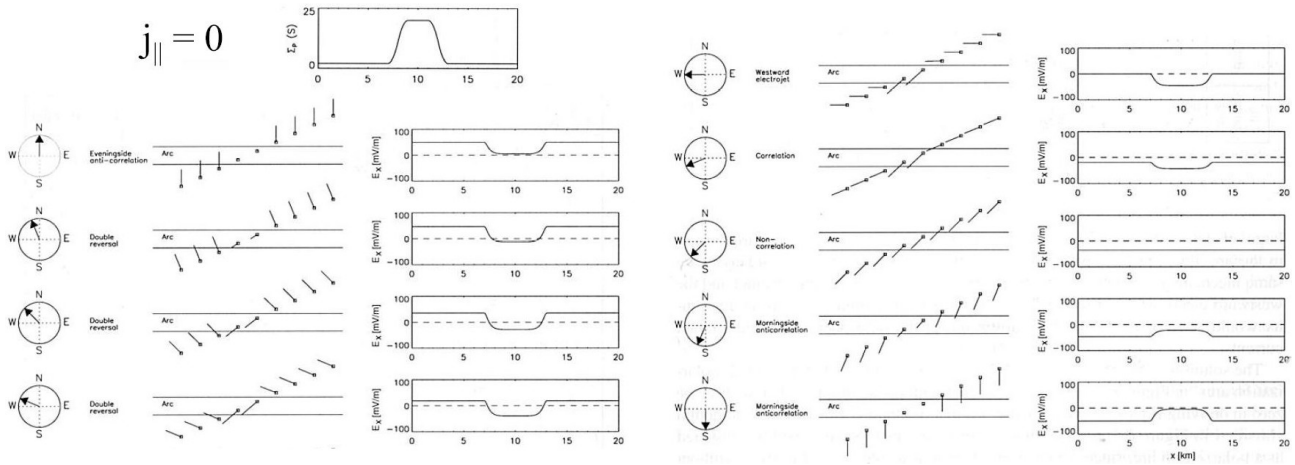

Figure 4. Numerical calculation of the arc-associated electric field, depending on the orientation of the background electric field, when $j_{\parallel} = 0$. After Figure 6.2 of *Paschmann et al.* [2003]. The top left panel shows the conductance profile used for the calculations. The other panels present electric field results. Each line shows the direction of the electric field, a name for the respective pattern (according to Table 1 of *Marklund* [1984]), a vector plot of the electric field across the arc, and the poleward component of the electric field, E_x, as provided by equation (16). Note that the direction normal to the arc is labeled x instead of ξ. The background electric field is equal to 50 mV/m and its direction is varied from poleward to equatorward via westward in steps of 22.5°.

Figures 4 and 5. Depending on the orientation of the background electric field with respect to the arc and on the magnitude of the FAC, the electric field and conductance patterns associated with the arc can be correlated, anti-correlated, or non-correlated, with various degrees of asymmetry.

For the polarization arcs (Figure 4), the electric field in equation (16) is dominated by the first (Pedersen) or second (Hall) term. In this case, sharp conductance gradients, e. g. at the edges of the arc, are associated with build up of polarization charge, because part of the intense current inside the arc cannot be transported to the low conductance ionosphere outside of the arc. The secondary electric field induced by the polarization charge serves to restore current continuity. Note that for a 'thin' ionosphere only the current carriers make the difference between the Pedersen and Hall term: ions moving along the electric field and electrons moving normal to the electric field, respectively.

For the Birkeland current arcs (Figure 5), the variation of the electric field is dominated by the third term in equation (16). The reader may feel confused by the fact that the FAC plays a key role in shaping the arc-associated electric field only for some of the arcs, while the increase in conductance inside the arc is always generated by FAC. However, the sheet current carried by the FAC is typically of the order of one to a few 0.1 A/m, while the ionospheric current can easily reach values of 1 A/m or larger (e. g. by an electric field of 50 mV/m and a conductance of 20 mho, which are certainly not extreme). Thus, even if the FAC drives the variation in conductance, the excess ionospheric current driving the build up of the polarization electric field can still be significantly larger than the ionospheric current closing the FAC. The third term in equation (16) dominates only when the ambient electric field is weak, for example near the convection reversal (CR) boundary. However, since the most structured and dynamic auroras are observed to occur near the CR, close to the polar cap boundary in the evening sector and in the Harang region (see Section 5) in the pre-midnight and midnight sectors, the fraction of Birkeland current arcs is certainly significant.

FAST observations [*Elphic et al.*, 1998] showed that broad upward currents associated with auroral arcs are often connected to narrow intense return currents, flowing at the side(s) of the arc. A synthetic scheme that emerged based on these observations is shown in Figure 6. In the return

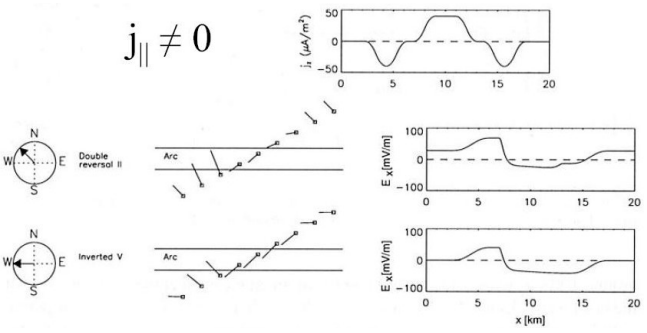

Figure 5. Numerical calculation of the arc-associated electric field for two cases of $j_{\parallel} \neq 0$. After Figure 6.5 of *Paschmann et al.* [2003]. The top panel shows the FAC profile, while the conductance and the format of the electric field results are the same as in Fig. 4.

current region the plasma density is decreased (because both the electrons and the ions move away, as carriers of the downward FAC and Pedersen current, respectively [e. g. *Karlsson and Marklund*, 1998]), therefore the electric field overshoots the background level, to keep the current continuous [e. g. *Aikio et al.*, 1993]. This effect is reflected also by the first r.h.s. term of equation (16), if Σ_P is smaller than Σ_{P_0}. Note that the electric field overshoot visible in Figure 5 is required to carry the enhanced ionospheric current fed by the downward FAC; the intensification due to plasma depletion comes on top.

3.2. Auroral current circuit

While polarization and FAC provide the two basic mechanisms to ensure current continuity in the ionosphere, their relative importance in a specific event depends not only on ionospheric processes, but also on M–I coupling details. The *Type 1* configuration of the auroral current circuit suggested by *Boström* [1964] (Figure 7) emphasizes the polarization, required to compensate the FAC blockage above the arc, while for *Type 2* current continuity relies on FAC sheets closing across the arc. Although some of the features associated with the two configurations were in the meanwhile revised (like the missing field-aligned potential drop for *Type 2*), the points made by *Boström* [1964] proved to be essentially correct — at a time when the existence of field-aligned currents was still doubted!

An outstanding illustration of the *Type 1* configuration is provided by the substorm current wedge [*McPherron et al.*, 1973], while the large scale 'Region 1' and 'Region 2' FAC [*Iijima and Potemra*, 1976], or the smaller scale arc current system illustrate the *Type 2*. The correlation between E_ξ and H_η, sometimes very high [e. g. *Sugiura*, 1984], is an effect of the *Type 2* configuration and an immediate consequence of equation (16), provided that the third term prevails and Σ_P is constant (this assumption is of course questionable in darkness, but some correlation may still survive on oval scale).

The fundamental question of quantifying the relationship between polarization and FAC was addressed from an M–I coupling perspective by *Lysak* [1986], who provided a unifying framework including both the time varying ionosphere, the dynamic and non-uniform flux tube, and the magnetospheric generator. *Lysak* [1986] integrated former results on the ionospheric feedback and its effect upon the development of the auroral arc [*Sato*, 1978, and references therein] and upon the westward traveling surge [*Rothwell et al.*, 1984] — explaining, for example, the fast motion of the aurora during substorms. *Lysak* [1986] was also able to show that for short time scales, shorter than

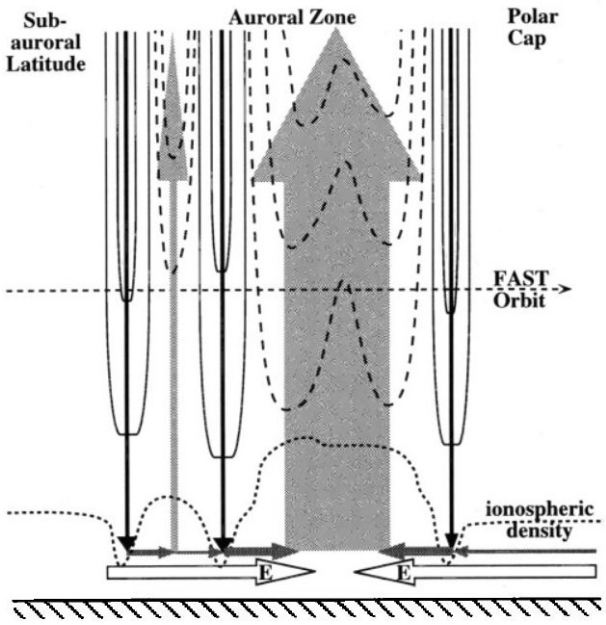

Figure 6. The low altitude end of the auroral current circuit, including broad upward FAC and narrow downward FAC regions, ionospheric FAC closure by Pedersen currents, density depletions associated with the downward FAC, and AAR equipotential contours in both FAC regions. After *Elphic et al.* [1998].

~1 min (equal to the Alfvén travel time from the ionosphere to the magnetospheric generator and back), the feedback instability is governed by the ionosphere interaction with the non-uniform flux tube. Considering the ionospheric reflection coefficient of the Alfén wave, $R = (\Sigma_A - \Sigma_P)/(\Sigma_A + \Sigma_P) \simeq -1$ (because $\Sigma_A \simeq 1$ mho, the Alfvén wave admittance, is in general much smaller than $\Sigma_P \simeq 10$ mho), the auroral arc can be regarded as almost completely polarized on such short time scales. A variation in the electric field carried by an incoming Alfvén wave is canceled by the induced polarization associated with the reflected wave. Such rapid variations, however, are beyond the scope of the present review.

On longer time scales, as soon as the equilibrium of the M–I system is achieved, the relationship between polarization and FAC depends on the specific features of the magnetospheric generator. A possible way to model the generator is by attributing it a Pedersen type conductance Σ_G [*Lysak*, 1985], whose variation between very small ($\Sigma_G \ll \Sigma_P$) and very large ($\Sigma_G \gg \Sigma_P$) values is equivalent to a smooth change from a purely current to a purely voltage generator. In the first case, demonstrated to fit better with smaller scales, the ionospheric electric field has to adjust — by polarization — to the variation of the ionospheric conductance, in order to match the FAC imposed from the magnetosphere. In the second case, better suited to larger scales, the electric field is fixed, and

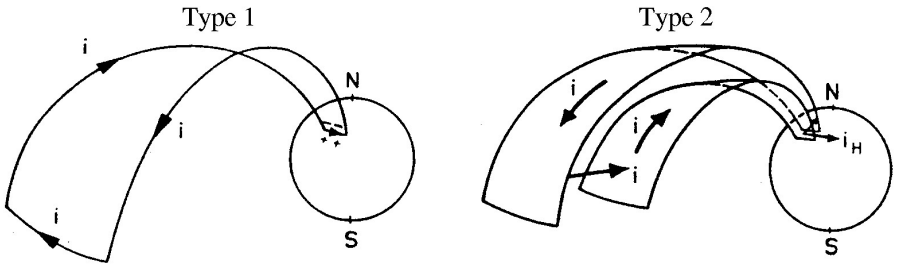

Figure 7. The two configurations of the auroral current circuit predicted by *Boström* [1964].

the variation of ionospheric conductance results in the modification of the ionospheric current, feeding or being fed by FAC. Of course, in specific events, neither the characteristics of the generator, nor the actual relationship between polarization and FAC, are known beforehand.

4. THICK UNIFORM 2D ARC

When a fraction of the polarization build up is driven by the tangential electric field, fourth r.h.s. term in equation (12), the electrojet along the arc (or, in general, along the high conductivity channel), can become much larger than the current driven by the primary electric field. Assuming a configuration with the primary electric field in tangential direction, E^p_η, this will drive a primary Pedersen current along the arc, $J^p_{\eta_P} = \Sigma_P E^p_\eta$, and a primary Hall current across the arc, $J^p_{\xi_H} = \Sigma_H E^p_\eta$. If there is no discharge of the polarization by FAC (that is, if the efficiency of the Cowling mechanism is $\alpha_C = 1$, see below), the secondary electric field associated with the charge build up, E^s_ξ, drives a secondary Pedersen current that balances the primary Hall current, $J^s_{\xi_P} = \Sigma_P E^s_\xi = \Sigma_H E^p_\eta$. At the same time, E^s_ξ drives a secondary Hall current along the arc, $J^s_{\eta_H} = \Sigma_H E^s_\xi = (\Sigma^2_H/\Sigma_P)E^p_\eta$, that adds to the primary Pedersen current, such that the total current becomes:

$$J_\eta = J^p_{\eta_P} + J^s_{\eta_H} = \Sigma_P(1 + (\Sigma_H/\Sigma_P)^2)E^p_\eta = \Sigma_C E_\eta \tag{17}$$

with Σ_C the Cowling conductivity. If the ratio Σ_H/Σ_P is large enough, the Cowling effect can enhance the effective conductance by an order of magnitude (e.g. $\Sigma_C/\Sigma_P = 10$ for $\Sigma_H/\Sigma_P = 3$).

While this textbook explanation of the Cowling effect assumes that the polarization discharge by FAC is completely blocked, in reality both the polarization and FAC contribute (as before) to the current closure. The efficiency of the Cowling mechanism is defined, in general terms, by [e.g. *Amm et al.*, 2011]:

$$\nabla \cdot \mathbf{J}^s_P = -\alpha_C \nabla \cdot \mathbf{J}^p_H \tag{18}$$

where $\alpha_C = 1$ corresponds to complete FAC blockage and $\alpha_C = 0$ implies that the primary Hall current is fully coupled to the FAC. The situations in between, $0 < \alpha_C < 1$, correspond to a partial Cowling channel.

In order to understand the details of the current closure associated with a partial Cowling channel, one has to take into account that the Pedersen and Hall currents have different altitudinal profiles (Figure 3). In the model proposed by *Fujii et al.* [2011], the two currents flow in two thin sheets separated in altitude (Figure 2c), and a fraction α_C of the diverging primary Hall current feeds an ionospheric loop closed by the secondary Pedersen current. For $\alpha_C = 1$ the divergence of the Hall current is fully closed in the ionospheric loop, while for $\alpha_C = 0$ there is no ionospheric loop and the diverging Hall current is fully coupled to the FAC. Note that an observed $\alpha_C = 0$ may also mean that the Hall current is actually divergence free, therefore the Cowling mechanism is absent (see below).

The FAC coupling to the Hall current associated with a partial Cowling channel raises also the problem of the energy flow. While the Poynting flux carried by the FAC cannot be dissipated by the Hall current, the model advanced by *Fujii et al.* [2011] explains how the energy is eventually dissipated by the secondary Pedersen current. An apparent difficulty of this process is that in a complete Cowling channel, $\alpha_C = 1$, there is no FAC energy supply to feed the dissipation. However, in a time dependent framework energy build up and energy consumption are not necessarily simultaneous. As a matter of fact, *Fujii et al.* [2011] assume electrostatic conditions, which implies that the energy build up process has already occurred [*Yoshikawa*, 2002a, b]. The complete Cowling channel can still dissipate the energy accumulated during the build up phase.

An outstanding example of Cowling channel is the equatorial electrojet [*Chapman*, 1956]. In this case, polarization charge builds up because the vertical Hall current is prevented to flow outside of the ionospheric layer. However, in the auroral ionosphere the configuration is different, with more elusive limitations of the Hall current flow at the

"edges" of the arc or electrojet. Similar to the relationship between FAC closure by Pedersen currents and polarization, discussed in the previous Section, the efficiency of the Cowling mechanism depends not only on ionospheric processes, but also on the magnetospheric end of the current circuit. While a comprehensive theory is not available yet, experimental evidence obtained by *Amm et al.* [2011] indicates that the Cowling efficiency is likely to be correlated with the activity level. Since the Cowling mechanism relies on the diverging component of the Hall current, this study confirms also that the Hall current is essentially divergence free during quiet times.

Even if *Amm et al.* [2011] address meso-scale features, based on radar and ground magnetic field data, it is reasonable to think that the Cowling mechanism operates also on arc scales, and shows a similar correlation with arc related "activity". Since meso-scale activity, quantified by the magnetic disturbance, scales with the energy dumped in the ionosphere, the efficiency of the Cowling mechanism on arc scale may well be related to the energy flux of the precipitating electrons.

5. THIN NON-UNIFORM 2D ARC

In this Section the exploration of equation (12) continues with the terms that depend on variations in η, because of non-uniformity along the arc. We concentrate on the variations in conductance and neglect the variation in the electric field, $\partial E_\eta/\partial\eta$, which contributes to polarization. While this contribution can be important near the ends of the arc, its effect is presumably small in rest, where the polarization associated with $\partial E_\xi/\partial\xi$ dominates. Following *Marghitu et al.* [2004, 2009, 2011], we introduce a simple 2D arc model, whose key difference with respect to the 1D model is the diverging electrojet. The model is implemented by the ALADYN technique and illustrated with an arc event in the Harang region. A number of features of the ionospheric current closure are then explored by a semi-quantitative approach.

5.1. Model, technique, event study

5.1.1. Model and technique

If the source free electrojet, $\partial J_\eta/\partial\eta = 0$, is replaced with a divergent electrojet, $\partial J_\eta/\partial\eta = c_1 \neq 0$, where c_1 is assumed constant in normal direction, the current continuity equation (10) becomes:

$$j_\parallel - \frac{\partial J_\xi}{\partial\xi} = \frac{\partial J_\eta}{\partial\eta} = c_1 \tag{19}$$

which yields, by integration along ξ:

$$H_\eta - J_\xi = c_0 + c_1\xi \tag{20}$$

Both c_0 and c_1 are assumed independent of η, assumption motivated in particular for satellites on polar orbits, crossing the arc (and oval) typically close to normal direction. In this case the satellite displacement along the arc is small compared to the length scale of the electrojet, and c_0, c_1 can indeed be considered as constant.

While equation (20) is very similar to the 1D equation (15) and the formal electric field solution can be easily obtained, the term $c_1\xi$ introduces one more degree of freedom, that makes obtaining actual values for the electric field more difficult. In addition, the tangential electric field, E_η, is not always known (which may raise difficulties also for the 1D arc model, equation (16)).

Observed satellite data can be processed by the ALADYN (**a**urora**l** **a**rc electro**dyn**amics) technique, introduced by *Marghitu et al.* [2004] and updated by *Marghitu et al.* [2011]. As before, Ohm's law is used to replace J_ξ and E_η is constant, $E_\eta = b_0$. In addition, E_x is expressed as a series expansion:

$$E_x = E_{0_x} + \sum_{i=1}^{n_x} a_i G_i \tag{21}$$

where G_i is the Legendre polynomial of order i and E_{0_x} is the average ionospheric electric field, $E_{0_x} = \int E_x dx/L$ (with E_x the measured electric field and L the mapped length of the satellite path). As compared to Section 3, the electric field at some initial point is replaced by the more robust average electric field, whose error is smaller (because the error of the average is smaller than the error of individual data points). The order n_x of the series expansion depends on the conductance profile, with larger values needed for higher variability of the conductance (within the constraint of the data resolution).

With simple algebra, equation (20) is cast into:

$$\frac{\Sigma_P}{\cos\theta}\sum_{i=1}^{n_x} a_i G_i - (\Sigma_H - \Sigma_P\tan\theta)b_0 + c_0 + c_1 x\cos\theta = H_y\cos\theta - H_x\sin\theta - \frac{\Sigma_P E_{0_x}}{\cos\theta} \tag{22}$$

where $\Sigma_P, \Sigma_H, E_{0_x}, H_x, H_y$ can be inferred from the measured data and the parameters (a_i, b_0, c_0, c_1) can be, in principle, derived by fit. Note that when b_0 and c_1 are fixed, equation (22) provides an approximation (whose accuracy depends on n_x) of the unique E_x solution and unique c_0 constant, in the same way as equation (16) provides the unique E_x solution when $E_\eta \equiv b_0$ is fixed.

In practice, the fit equation (22) is solved by assuming a divergence free electrojet, $c_1 = 0$, for a set of different b_0 values, over a sliding window moved at a certain time step. For each b_0 one obtains

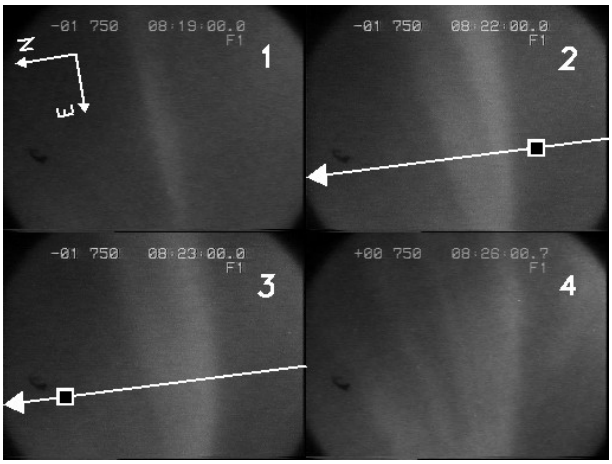

Figure 8. Arc event analyzed by ALADYN. The four selected frames show a stationary arc during the ∼1 min FAST overpass, but a gradual development on a ∼10 min time scale. After *Marghitu et al.* [2011].

thus a sliding series of fitted electric field solutions, E_x^f, whose root mean square difference against the (mapped) measured electric field, E_x^m, is computed as δE_x. At the same time, one obtains also a sliding series of c_0 values, that can be used to check the divergence of the electrojet, $c_1 = \Delta c_0/\Delta x \cos\theta$, depending as well on b_0. A positive / negative variation of c_0 indicates a positive / negative divergence of the electrojet. As demonstrated below, the two sets of profiles, δE_x and c_0, provide also an indication on the most likely range for b_0.

While the ALADYN technique enables the examination of 2D arc (and oval) features, the assumptions made still require an elongated geometry and reasonable steady state conditions — at least on time scales comparable to the width of the sliding window, $\gtrsim$10 s. The geometry and dynamics of the aurora can be best judged from conjugate optical data, but ground and *in-situ* magnetic field data may also provide this information (however, with less accuracy). ALADYN results can also suffer from errors in conductance (in particular when the conductance is low), significant neutral winds, errors in the arc inclination θ, and arc curvature significantly larger than the curvature of the latitude circle [*Marghitu et al.*, 2011].

5.1.2. Event Study: FAST Orbit 1859

Figures 8 and 9 summarize optical and FAST data, together with ALADYN results, for a relatively quiet evening event, observed during the growth phase of a small substorm [*Marghitu et al.*, 2009, 2011]. An outstanding feature of this event is the close proximity of the convection reversal (CR) and FAC reversal boundaries, both of which are encountered near 8:22 (Figures 9d and 9e). This configuration prevents the standard Type 2 current closure and requires FAC coupling to the electrojets, a qualitative result which is substantiated by the ALADYN analysis. At the same time, an (weaker) eastward and a (stronger) westward electrojet flow equatorward and poleward of the CR, respectively, indicating an event observed in the Harang region.

Figures 9f and 9g show δE_x and c_0 depending on b_0, as obtained over a sliding window of 15 s moved in steps of 1 s (similar results were obtained for windows of 10 and 20 s). In each plot, b_0 is varied from -40 to 20 mV/m, in steps of 5 mV/m, including presumably the actual value of the tangential electric field (typically small and negative). A priori, when varying b_0 from -40 mV/m (westward) to 20 mV/m (eastward), a minimum in δE_x is expected to correspond to the actual b_0. When the conductance is large, and the results more accurate, this is indeed the case, with the minimum δE_x reached for the cyan–green lines (b_0 from -20 to 0 mV/m). However, a certain amount of variability is always associated with c_0, in the range of 0.1–0.2 A/m. This is comparable to the FAC sheet current, and therefore significant. According to equation (15), one can conclude that $H_\eta - J_\xi$ varies along the satellite footpoint, which implies a diverging electrojet.

The dependence of the overall fit quality and c_0 variability on b_0 can be examined closer in Figures 9h and 9i, which indicate that both parameters reach their minima for b_0 between -20 and -10 mV/m. Figure 9j shows the associated three profiles of c_0. The average electrojet divergence over the time intervals corresponding to the downward and upward FAC, roughly 8:19–8:22 and 8:22–8:23, are equal to about 0.2 A/m / 480 km $\simeq$ 0.4 μA/m^2 and $-$0.2 A/m / 160 km $\simeq$ -1.3 μA/m^2. These values are in good agreement with the respective FAC densities, suggesting that, on average, the downward FAC feeds the eastward electrojet, while the upward FAC is fed by the westward electrojet. Figure 9j shows also that a small change in b_0 can result in a significant variation of the small scale current structure where the conductance is high. However, the effect on the large scale trend is rather limited.

At the peak of Σ_H, from 8:22:10–8:22:20, c_0 has an abrupt decrease of ∼0.1 A/m. This value is comparable to the decrease of the FAC H_p in Figure 9e and corresponds to a current density of ∼3.3 μA/m^2. At this time $\Sigma_P \simeq 15$ mho (Fig. 9c), therefore the Pedersen tangential current is $J_{\eta P} \simeq 0.15$ A/m, assuming $E_\eta \simeq -10$ mV/m. If the electrojet divergence were achieved only at the expense of the Pedersen current, its variation length scale should be equal to about 0.15 A/m / 3.3 μA/m^2, that is some 50 km. This length appears to be quite short, suggesting that the tan-

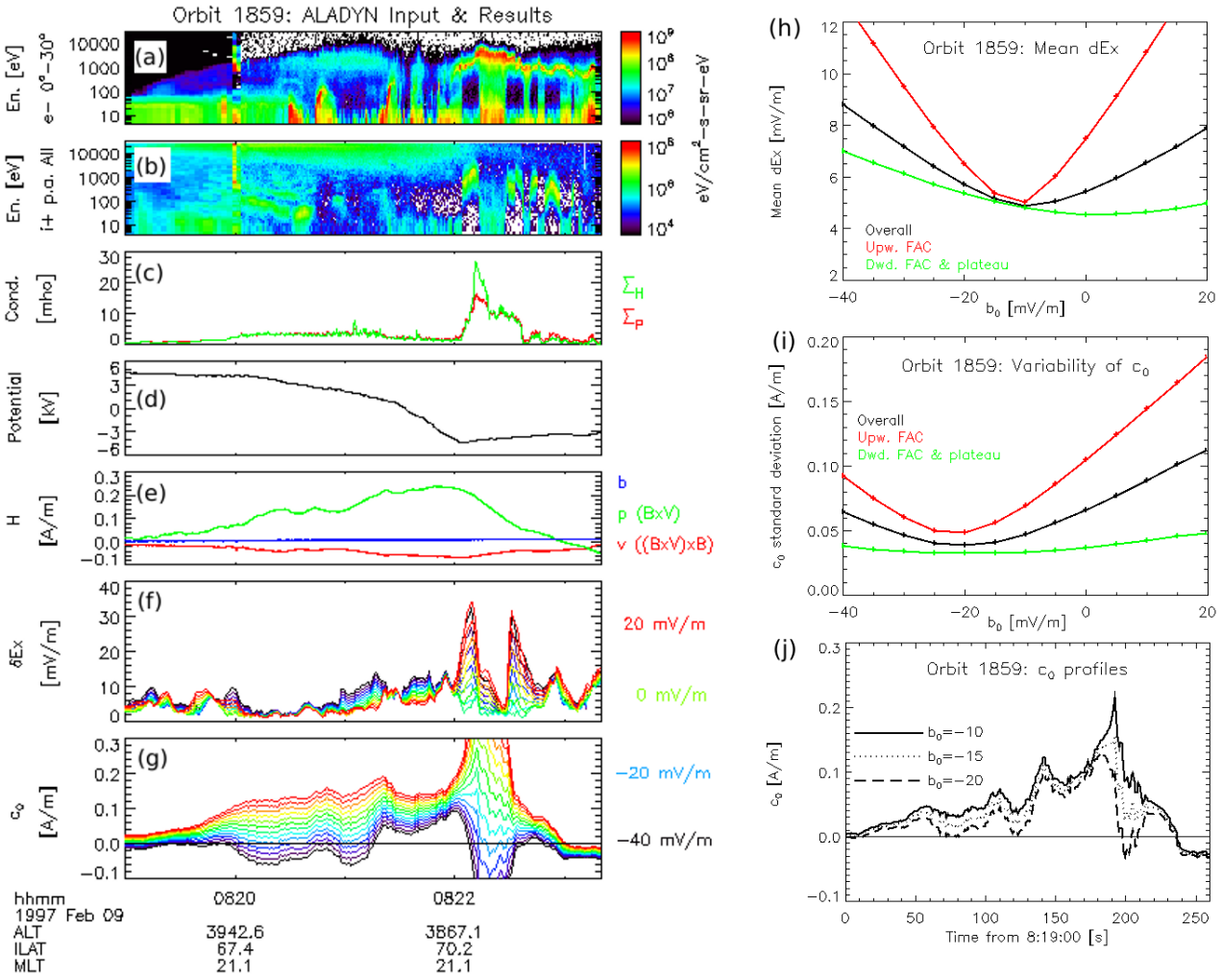

Figure 9. FAST data conjugate with the arc in Figure 8 together with ALADYN results. After Figures 3 and 4 from *Marghitu et al.* [2011]. *(a)–(e):* FAST data. (a) Electron and (b) ion time–energy spectrograms; (c) Pedersen and Hall conductance; (d) ionospheric potential along the FAST footpoint; (e) magnetic field perturbation. *(f)–(j):* ALADYN results. (f, g) δE_x and c_0 for b_0 between -40 and 20 mV/m, varied in steps of 5 mV/m; (h, i) Mean δE_x and the standard deviation of c_0, computed for each line in (f) and (g), respectively, over the whole FAC region (black), upward FAC (red), and downward FAC (green); (j) The c_0 profile for $b_0 = -20$, -15, and -10 mV/m.

gential Hall current may contribute as well to the FAC closure, a point to be explored further below.

5.2. Ionospheric current closure

If the polarization charge associated with $\partial E_\eta/\partial\eta$ is negligible, as assumed also by ALADYN, the divergence of the electrojet is caused by longitudinal gradients in conductance. If one can assume in addition that the FAC (and the number flux, Φ_N) is uniform along η, then according to equations (6) and (7) the gradients in conductance depend solely on the variation with η of the average particle energy, $\overline{E}(\eta)$. This second assumption is often supported by the magnetic field signature, consistent with a current sheet geometry (e. g. for FAST orbit 1859 explored above). Since structured aurora is more commonly associated with electron precipitation, we concentrate here on the electron induced conductance, equations (6), but a similar approach is possible also for proton precipitation.

With $\Phi_E = \overline{E}\Phi_N$, equations (6) write:

$$\begin{aligned} \Sigma_P^e &= \frac{40\overline{E}^{1.5}}{16+\overline{E}^2}\Phi_N^{1/2} \\ \Sigma_H^e &= \frac{18\overline{E}^{2.35}}{16+\overline{E}^2}\Phi_N^{1/2} \end{aligned} \tag{23}$$

For a given orientation of the electric field, E_η/E_ξ, the Pedersen and Hall components of the electrojet become (disregarding the sign):

$$\begin{aligned} |J_{\eta P}| &= \Sigma_P|E_\xi||E_\eta/E_\xi| \\ |J_{\eta H}| &= \Sigma_H|E_\xi| \end{aligned} \tag{24}$$

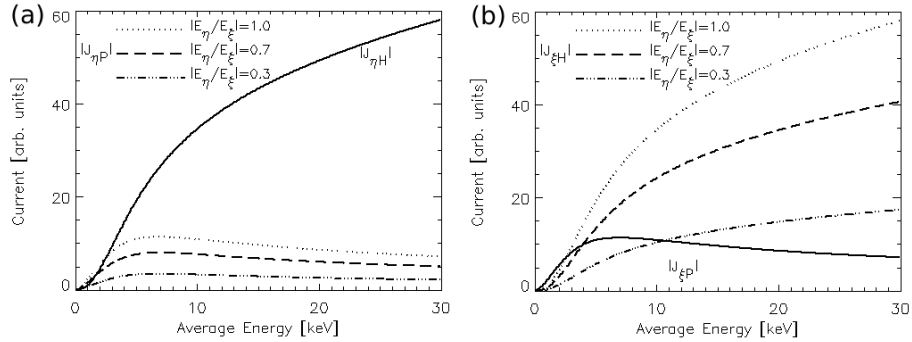

Figure 10. The relative contributions of the Pedersen and Hall components (absolute values) to the (a) longitudinal and (b) meridional current, depending on electron energy. After *Marghitu et al.* [2011], with energy range extended to 30 kV. It is assumed that the FAC (and number flux) is homogeneous in both directions, therefore the relative intensity of the currents $|J_{\xi P}|$, $|J_{\xi H}|$, $|J_{\eta P}|$, $|J_{\eta H}|$ depends only on the electron energy and on the ratio $|E_\eta/E_\xi|$. For $|E_\eta/E_\xi| = 1$, $|J_{\eta P}| = |J_{\xi P}|$ and $|J_{\eta H}| = |J_{\xi H}|$

After replacing Σ_P and Σ_H with the formulas (23) and dropping the common factors, $\Phi_N^{1/2}$ and E_ξ, the relative variation of $J_{\eta H}$ and $J_{\eta P}$ with $\overline{E}$ can be read in Figure 10a. The key information in this figure is that for electron energies above some 4–5 keV, $|dJ_{\eta H}/d\overline{E}| \gg |dJ_{\eta P}/d\overline{E}|$, therefore the divergence of the electrojet at high and moderate electron energies relies essentially on the Hall current. If the experimental evidence suggests FAC–EJ coupling, as it is the case for our FAST event, the FAC closure along the arc can only be achieved by Hall current. The association of this feature with higher electron energies is consistent with increased auroral activity and non-steady current flow.

To complete the exploration of the 2D current closure near the arc, one can compute the Pedersen and Hall components of J_ξ by the same procedure as for J_η. In this case:

$$\begin{aligned} |J_{\xi P}| &= \Sigma_P |E_\xi| \\ |J_{\xi H}| &= \Sigma_H |E_\xi| |E_\eta/E_\xi| \end{aligned} \tag{25}$$

and the results are presented in Figure 10b. This time the FAC is assumed to be uniform across the arc, assumption motivated when the FAC profile is smoother than the conductance profile (compare e. g. the variations of $j_\parallel$ in Figure 9e, as indicated by the changes in the slope of H_p, with the variations of the conductance in Figure 9c). The polarization, $\partial E_\xi/\partial\xi$, is again neglected. However, this condition is much stronger now, considering the sharper gradients across the arc. Although the polarization is less likely to be indeed negligible, Figure 10b still provides useful information.

The Pedersen current is seen to vary at low energies, as before, and to be relatively flat at higher energies. This does not mean that the Pedersen current cannot close the FAC at higher electron energies, but points out the importance of the neglected polarization in this energy range, corresponding to more disturbed conditions. Conversely, for low energies it appears that polarization is less critical for the Pedersen current closure. On the other hand, the information provided on the Hall current closure is rather limited. The variation of $J_{\xi H}$ in Figure 10b cannot be compared with the variation of $J_{\eta H}$ in Figure 10a because the variation length scales of $\overline{E}$ along ξ and η, $\lambda_\xi^{\overline{E}}$ and $\lambda_\eta^{\overline{E}}$, are not known.

However, a qualitative discussion of the Hall current divergence is still possible. If the electric field is electrostatic, a divergence free Hall current, as expected for quiet aurora, implies that the gradient of the Hall conductance is parallel to the electric field (see equation (11)). By ignoring the FAC non-uniformity and assuming that Σ_H depends solely on the electron energy, $\overline{E}$, this condition can be written as:

$$\frac{\lambda_\xi^{\overline{E}}}{\lambda_\eta^{\overline{E}}} \simeq \left|\frac{E_\eta}{E_\xi}\right| \tag{26}$$

where the partial derivatives were replaced by the variation length scales, $\partial/\partial(\xi,\eta) \simeq 1/\lambda_{\xi,\eta}^{\overline{E}}$.

If the tangential electric field is much smaller than the normal electric field, $E_\eta \ll E_\xi$, as expected in the evening and morning sectors, equation (26) indicates that quiet arcs are very elongated, consistent with observations. When the tangential electric field is significant, as expected in the Harang region (HR), equation (26) suggests that steady state arcs should be less elongated. An alternative interpretation is that a mismatch is more likely, therefore the Hall current is more likely to diverge and perhaps to couple with the FAC, in good agreement with the dynamic character of the HR. The auroral activity in the HR is thought to be closely related to the substorm onset [e. g. *Nielsen and Greenwald*, 1979; *Zou et al.*, 2009], even if the details of this relationship are not fully understood

[e. g. *Weygand et al.*, 2008]. Small scale perturbations in the magnetosphere, that drive locally the M–I system out of the steady state, can result in violations of equation (26). Such perturbations are related e. g. to bursty bulk flows, and recent observations that the substorm onset can be triggered by streamers that reach equatorward arcs in the HR [*Nishimura et al.*, 2010; *Lyons et al.*, 2010] are consistent with the alternative interpretation of equation (26).

6. OUTLOOK: TENTATIVE MODEL OF THE 3D ARC DURING SUBSTORM CYCLE

Based on the arc models in the previous Sections, a tentative scenario for the evolution of the 3D arc during the substorm cycle can be formulated as follows (see also *Marghitu et al.* [2011]):

1. The quiet arc is likely to be associated with a divergence free Hall current, little polarization, and FAC closure by Pedersen current. In the evening and morning sectors, where the electric field is mostly normal to the arc, the configuration of the auroral current circuit is of *Type 2* (Figure 7) and the arc can be described by the 1D model. In the Harang region, where the tangential electric field can be significant, the configuration can be mixed, *Type 1 / Type 2*, with FAC sheets (*Type 2*) connected to the Pedersen component of the electrojet (*Type 1*). In this case the 2D thin non-uniform model is required.

2. As soon as the substorm starts to grow, small amounts of polarization and Hall current divergence may begin to develop. At the same time, the divergence free Hall current can also grow slowly, associated with inductive build up of magnetic energy. Since growth phase arcs are typically located in the pre-midnight sector, in or near the Harang region, the electric field is likely to have a tangential component. Polarization and FAC can couple to both Pedersen and Hall current. At this stage, it may already be that some arc features can only be captured by a 3D model.

3. At onset and shortly afterward, most of the Hall current divergence may couple to the FAC, and the inductive build up of magnetic energy is strongly enhanced. Polarization may build up as well, in parallel with strong Alfvénic activity. Only a 3D model can fully describe the onset arc.

4. Later on, during the expansion phase, polarization plays a major role and a complete Cowling channel may develop along the arc. The dynamics of such a process is still to be unveiled and represents another challenge for the 3D arc model.

5. During the recovery phase, the M–I system returns to steady state and the energy stored inductively is dissipated. The Cowling channel may survive for a while, but with less and less Hall current divergence to feed the polarization. Eventually, the arcs can again be described by the simple 1D or 2D models.

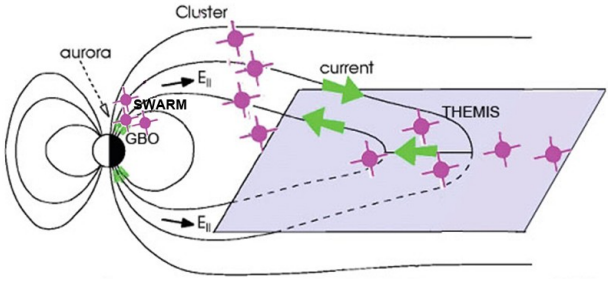

Figure 11. Sketch of the Swarm, Cluster, and THEMIS spacecraft, probing respectively the low altitude I–T, the topside AAR (indicated by $E_{\parallel}$), and the inner plasma sheet.

As mentioned already in Section 2.2, advanced techniques based on ground observations have opened new possibilities to study aurora, and are expected to contribute also to the understanding of the 3D arc. Significant advances in this direction are expected as well from the upcoming three-satellite Swarm mission, scheduled for launch at mid 2012. With two satellites on parallel orbits at ∼490 km and a third satellite at ∼530 km, Swarm will make possible a close examination of the ionospheric current closure associated with aurora. The two side-by-side Swarm spacecraft will provide a platform for systematic investigations of the gradients along the arc, while all three satellites, when flying in close formation, will enable studies of 2D auroral electrodynamics, including effects on the M–I–T coupling. One effect less studied so far is the influence of the neutral winds, in particular in sensitive regions with small electric fields, like the vicinity of the convection reversal boundary. The low altitude data provided by Swarm will complement the observations made by Cluster near the topside AAR and by THEMIS in the inner plasma sheet. Thus, multi-point data will be available from all the key regions of the auroral current circuit (Figure 11): the generator region (probed by THEMIS), the AAR (probed by Cluster), and the I–T load (probed by Swarm and ground based observatories).

7. SUMMARY

On time scales long enough to ignore inductive effects, auroral arc electrodynamics is controlled by current closure and Ohm's law. The details of the current closure, achieved by polarization and FAC, depend both on ionospheric and magnetospheric processes. While the ionospheric processes can be described with a certain accuracy, the magnetospheric end of the auroral current circuit is still

poorly understood. Arc models in one or two dimensions are able to capture some of the observed ionospheric features, but a complete 3D description is still to be developed. New ground based techniques and satellite missions will help in reaching this goal.

ACKNOWLEDGMENTS. The author is pleased to acknowledge fruitful discussions at the International Space Science Institute (ISSI), Bern, in the framework of the POLARIS team project. The work at ISS Bucharest was supported by the project ECSTRA, ESA Contract 4200098048, carried on under the PECS programme, and by the M–ICAR grant of the Romanian National Authority for Scientific Research, CNCS–UEFICDI, project number PN-II-ID-PCE-2011-3-1013.

REFERENCES

Aikio, A., H. Opgenoorth, M. Persson, and K. Kaila, Ground-based measurements of an arc-associated electric field, *J. Atmos. Terr. Phys.*, *55*, 797–808, 1993.

Amm, O., R.Fujii, K. Kauristie, A. Aikio, A. Yoshikawa, A. Ieda, and H. Vanhamäki, A statistical investigation of the Cowling channel efficiency in the auroral zone, *J. Geophys. Res.*, *116*, A02,304, doi:10.1029/2010JA015,988, 2011.

Amm, O., et al., Towards understanding the electrodynamics of the 3-dimensional high-latitude ionosphere: present and future, *Ann. Geophys.*, *26*, 3913–3932, 2008.

Atkinson, G., Auroral arcs: Result of the interaction of a dynamic magnetosphere with the ionosphere, *J. Geophys. Res.*, *75*, 4746–4755, 1970.

Baumjohann, W., Ionospheric and field-aligned current systems in the auroral zone: A concise review, *Adv. Space Res.*, *2*, 55–62, 1983.

Boström, R., A model of the auroral electrojets, *J. Geophys. Res.*, *69*, 4983–4999, 1964.

Brekke, A., and J. Moen, Review paper — Observations of high latitude ionospheric conductances, *J. Atmos. Terr. Phys.*, *55*, 1493–1512, 1993.

Brekke, A., S. Nozawa, and T. Sparr, Studies of the *E* region neutral wind in the quiet auroral ionosphere, *J. Geophys. Res.*, *99*, 8801–8825, 1994.

Chapman, S., The electrical conductivity of the ionosphere: A review, *Nuovo Cimento*, *[10]4* (Suppl. 4), 1385–1412, doi:10.1007/BF02746,310, 1956.

Coroniti, F., and C. Kennel, Polarization of the auroral electrojet, *J. Geophys. Res.*, *77*, 2835–2851, 1972.

de la Beaujardière, O., R. Vondrak, and M. Baron, Radar observations of electric fields and currents associated with auroral arcs, *J. Geophys. Res.*, *82*, 5051–5062, 1977.

Elphic, R., et al., The auroral current circuit and field-aligned currents observed by FAST, *Geophys. Res. Lett.*, *25*, 2033–2036, 1998.

Evans, D., N. Maynard, J. Troim, T. Jacobsen, and A. Egeland, Auroral vector electric field and particle comparisons 2. Electrodynamics of an arc, *J. Geophys. Res.*, *82*, 2235–2249, 1977.

Fuji, R., R. Hoffman, P. Anderson, J. Craven, M. Sugiura, L. Frank, and N. Maynard, Electrodynamic parameters in the nighttime sector during auroral substorms, *J. Geophys. Res.*, *99*, 6093–6112, 1994.

Fujii, R., O. Amm, A. Yoshikawa, A. Ieda, and H. Vanhamäki, Reformulation and energy flow of the Cowling channel, *J. Geophys. Res.*, *116*, A02,305, doi:10.1029/2010JA015,989, 2011.

Galand, M., and A. Richmond, Ionospheric electrical conductances produced by auroral proton precipitation, *J. Geophys. Res.*, *106*, 117–125, 2001.

Harang, L., The mean field of disturbance of polar geomagnetic storms, *Terrest. Magn. Atm. Electr.*, *51*, 353–380, 1946.

Heppner, J., The harang discontinuity in auroral belt ionospheric currents, *Geofys. Publ.*, *29*, 105, 1972.

Iijima, T., and T. Potemra, The amplitude distribution of field-aligned currents at northern high latitudes observed by Triad, *J. Geophys. Res.*, *81*, 2165–2174, 1976.

Kaeppler, S., et al., Current closure in the ionosphere, *this volume.*

Kamide, Y., On current continuity at the Harang discontinuity, *Planet. Space Sci.*, *26*, 237–244, 1978.

Karlsson, T., and G. Marklund, Simulations of effects of small-scale auroral current closure in the return current region, *Physics of Space Plasmas*, *15*, 401, 1998.

Kelley, M., *The Earth's Ionosphere*, *International Geophysics Series*, vol. 43, Academic Press, San Diego, California, 1989.

Kertz, W., *Einführung in die Geophysik. II. Obere Atmosphäre und Magnetosphäre*, *Hochschultaschenbücher*, vol. 535, Bibliographisches Institut, Mannheim, 1971.

Koskinen, H., and T. Pulkkinen, Midnight velocity shear zone and the concept of Harang discontinuity, *J. Geophys. Res.*, *100*, 9539–9547, 1995.

Lanchester, B., N. Ivchenko, B. Gustavsson, D. Whiter, H. Dahlgren, B. Goodbody, and G. Marklund, Imaging of aurora to estimate the energy and flux of electron precipitation, *this volume.*

Lyons, L., Y. Nishimura, Y. Shi, S. Zou, H.-J. Kim, V. Angelopoulos, C. Heinselman, M. Nicolls, and K.-H. Fornacon, Substorm triggering by new plasma intrusion: Incoherent-scatter radar observations, *J. Geophys. Res.*, *115*, A07,223, doi:10.1029/2009JA015,168, 2010.

Lyons, L., et al., Interplay of large and mesoscale structure of electrodynamical magnetosphere–ionosphere coupling, *this volume.*

Lysak, R., Auroral electrodynamics with current and voltage generators, *J. Geophys. Res.*, *90*, 4178, 1985.

Lysak, R., Coupling of the dynamic ionosphere to auroral flux tubes, *J. Geophys. Res.*, *91*, 7047–7056, 1986.

Marghitu, O., B. Klecker, G. Haerendel, and J. McFadden, ALADYN: A method to investigate auroral arc electrodynamics from satellite data, *J. Geophys. Res.*, *109*, A11,305, doi:10.1029/2004JA010,474, 2004.

Marghitu, O., T.Karlsson, B. Klecker, G. Haerendel, and J. McFadden, Auroral arc and oval electrodynamics in the Harang region, *J. Geophys. Res.*, *114*, A03,214, doi:10.1029/2008JA013,630, 2009.

Marghitu, O., C. Bunescu, T.Karlsson, B. Klecker, and H. Stenbaek-Nielsen, On the divergence of the auroral electrojets, *J. Geophys. Res.*, *116*, A00K17, doi:10.1029/2011JA016,789, 2011.

Marklund, G., Auroral arc classification scheme based on the observed arc-associated electric field pattern, *Planet. Space Sci.*, *32*, 193–211, 1984.

Mauk, B., and F. Bagenal, Comparative auroral physics: Earth and other planets, *this volume.*

McPherron, R., C. Russell, and M. Aubry, Satellite studies of magnetospheric substorms on August 15, 1968. 9. Phenomenological model for substorms, *J. Geophys. Res.*, *78*, 3131–3149, 1973.

Nielsen, E., and R. Greenwald, Electron flow and visual aurora at the Harang discontinuity, *J. Geophys. Res.*, *84*, 4189–4200, 1979.

Nishimura, Y., L. Lyons, S. Zou, V. Angelopoulos, and S. Mende, Substorm triggering by new plasma intrusion: THEMIS all-sky imager observations, *J. Geophys. Res.*, *115*, A07,222, doi:10.1029/2009JA015,166, 2010.

Nozawa, S., and A. Brekke, Studies of the *E* region neutral wind in the disturbed auroral ionosphere, *J. Geophys. Res.*, *100*, 14,717–14,734, 1995.

Paschmann, G., S. Haaland, and R. Treumann (Eds.), *Auroral plasma physics*, no. 15 in Space Science series of ISSI, Kluwer, Dordrecht, 2003.

Ray, L., and R. Ergun, Auroral signatures of ionosphere–magnetosphere coupling at Jupiter and Saturn, *this volume*.

Robinson, R., R. Vondrak, K. Miller, T. Dabbs, and D. Hardy, On calculating ionospheric conductances from the flux and energy of precipitating electrons, *J. Geophys. Res.*, *92*, 2565–2569, 1987.

Rothwell, P., M. Silevitch, and L. Block, A model for the propagation of the westward traveling surge, *J. Geophys. Res.*, *89*, 8941–8948, 1984.

Sato, T., A theory of quiet auroral arcs, *J. Geophys. Res.*, *83*, 1042–1048, 1978.

Semeter, J., Coherence in auroral fine structure, *this volume*.

Stallard, T., Clues on ionospheric electrodynamics from IR aurora at Jupiter and Saturn, *this volume*.

Sugiura, M., A fundamental magnetosphere-ionosphere coupling mode involving field-aligned currents as deduced from DE-2 observations, *Geophys. Res. Lett.*, *11*, 877–880, 1984.

Untiedt, J., and W. Baumjohann, Studies of polar current systems using the IMS Scandinavian magnetometer array, *Space Sci. Rev.*, *63*, 245–390, 1993.

Vanhamäki, H., and O. Amm, Analysis of ionospheric electrodynamic parameters on mesoscale — a review of selected techniques using data from ground-based observation networks and satellites, *Ann. Geophys.*, *29*, 467–491, 2011.

Weygand, J., R. McPherron, H. Frey, O. Amm, K. Kauristie, A. Viljanen, and A. Koistinen, Relation of substorm onset to Harang discontinuity, *J. Geophys. Res.*, *113*, A04,213, doi:10.1029/2007JA012,537, 2008.

Yoshikawa, A., How does the ionospheric rotational hall current absorb the increasing energy from the field-aligned current system?, *Geophys. Res. Lett.*, *29(7)*, 1133, doi:10.1029/2001GL014,125, 2002a.

Yoshikawa, A., Excitation of a hall-current generator by field-aligned current closure, via an ionospheric, divergent hall current, during the transient phase of magnetosphere–ionosphere coupling, *J. Geophys. Res.*, *107(A12)*, 1445, doi:10.1029/2001JA009,170, 2002b.

Yoshikawa, A., A. Nakamizo, O.Amm, H. Vanhamäki, R. Fujii, Y.-M. Tanaka, T. Uozumi, K. Yumoto, and S. Ohtani, Self-consistent formulation for the evolution of ionospheric conductances at the ionospheric e-region within an m–i coupling scheme, *J. Geophys. Res.*, *116*, A09,223, doi:10.1029/2011JA016,449, 2011.

Zou, S., L. Lyons, C.-P. Wang, A. Boudouridis, J. Ruohoniemi, P. Anderson, P. Dyson, and J. Devlin, On the coupling between the Harang reversal evolution and substorm dynamics: A synthesis of SuperDARN, DMSP, and IMAGE observations, *J. Geophys. Res.*, *114*, A01,205, doi:10.1029/2008JA013,449, 2009.

Zou, S., L. Lyons, Y. Nishimura, M. Nicolls, S. Mende, and C. Heinselman, Mutual evolution of aurora and ionospheric electrodynamic features near the Harang reversal during substorms, *this volume*.

O. Marghitu, Institute for Space Sciences, P.O.Box MG-23, RO-77125 Bucharest-Măgurele, Romania
(marghitu@gpsm.spacescience.ro)